Composites: Part A 187 (2024) 108473

Contents lists available at ScienceDirect

Composites Part A

journal homepage: www.elsevier.com/locate/compositesa

Microstructural behavior of CNT-PDMS thin-films for multifunctional systems

Matthew Phillips, Pouria Zaghari, Jong Eun Ryu, Mohammed Zikry *

Department of Mechanical and Aerospace Engineering, North Carolina State University, Raleigh, NC 27695, USA

ARTICLE INFO

Keywords:
Ribbing
Hyperelasticity
Viscoelasticity
PDMS
Carbon-nanotube
Scanning electron microscopy
Fracture
Morphology

ABSTRACT

Heterogeneous ribbed and non-ribbed carbon nanotube (CNT)-PDMS thin-film systems manufactured by large-scale rolling exhibit large-strain and high strain-rate characteristics with favorable surface behaviors, such as superhydrophobicity and drag reduction. However, it is not well understood how the multi-phase microstructure and material properties of non-ribbed thin-films are related to the surface material behavior and fracture. Hence, the objective of this investigation is to characterize the large-strain mechanical behavior and the microstructure of various CNT-PDMS compositions to understand how the CNT loading, agglomeration, distribution, and orientation affect the mechanical behavior and fracture of CNT-PDMS unribbed systems. Non-ribbed thin tensile testing specimens were fabricated for neat PDMS and CNT-PDMS with different weight CNT distributions to understand non-ribbed behavior. The ultimate strain, strength, and global stress–strain behavior were obtained by uniaxial mechanical testing. Scanning electron microscopy (SEM) of the fracture surface was also obtained for each sample to analyze the microstructure and relate the damage mode to the different weight distributions. Based on these experimental measurements and observations, large-strain, hyperelastic and hyper-viscoelastic material models were used to characterize the material behavior. The hyper-viscoelastic material model was shown to provide the most accurate material description of the thin-film behavior of the viscoelastic PDMS with the high-strength CNTs.

1. Introduction

Ribbed carbon-nanotube-polydimethylsiloxane (CNT-PDMS) thin-film materials are multi-phase and heterogeneous systems that can exhibit favorable behaviors, such as superhydrophobicity, drag reduction, and anti-biofouling [1–7]. These systems exist in the broader area of bio-inspired materials and structures [1,7,8]. CNT-PDMS manufactured with a ribbed microstructure are one such bio-inspired system that exhibits hierarchal shark-skin-like surfaces that provide superhydrophobic and drag reducing properties. These heterogeneous materials are periodic surfaces that can be characterized by a ribbing amplitude (A), ribbing wavelength (λ), and film thickness (H) [1–3,5,9,10]. The structured thin-film system can be manufactured by large-scale rolling, which has the potential for continuous manufacturing and cost-effective mass production. Ribbing morphology can be designed and tailored by the manufacturing conditions, such as the roller speed, roller speed ratio, and the roller gap [2,3,5,9]. Ribbing microstructural parameters, such as the ribbing aspect ratio (α_r) and the ribbing length ratio (α_l), can be used to characterize the asperity and texture of the ribbing structure. The ribbing aspect ratio is the ribbing amplitude divided by the ribbing wavelength ($\alpha_r = A/\lambda$); the ribbing length ratio is the film thickness divided by the ribbing wavelength ($\alpha_l = H/\lambda$). These feature aspect ratios are used to characterize systems, such as wrinkled thin-films and structured topographical surfaces [5,11,12]. The non-dimensional ribbing microstructural parameters provide meaningful insights to understand and predict the film stress that accumulates during the rolling process and during extreme dynamic behavior [5]. However, before the mechanical behavior of the structured surface can be fully understood, a physically-based and accurate material model of non-ribbed CNT-PDMS systems must be characterized, such that a fundamental understanding of CNT-PDMS can be fully understdood.

PDMS, as with most polymers, exhibits a degree of time- or rate-dependent viscoelastic relaxation that results from the reversible stretching of polymer chains and is capable of achieving large strains [13–21]. The addition of CNTs increases the strength of the material by preventing the movement of polymer chain entanglements. Most material characterization and modeling of PDMS and CNT-PDMS has been

* Corresponding author.
E-mail address: zikry@ncsu.edu (M. Zikry).

https://doi.org/10.1016/j.compositesa.2024.108473
Received 11 July 2024; Received in revised form 29 August 2024; Accepted 11 September 2024
Available online 12 September 2024

limited to small-strain viscoelastic behavior using dynamic mechanical analysis or creep tests and Prony series viscoelastic material models [2,3,5,19,22–24]. The Prony series representation can be converted between time-dependent and frequency-dependent forms, such that the material model can be obtained from either creep tests (time domain) or dynamic mechanical analysis (frequency domain), and it can then be used to predict the behavior in the other domain [15,25].

When subjected to large strains, additional deformation modes of the polymer chains occur that can result in hyperelastic behavior [22,23,26–31]. Many hyperelastic material models exist in the literature, each of which is tailored for different materials or strain regimes. A recent review [26] found that the Ogden, Yeoh, Carroll, and Shariff hyperelastic material models have a coefficient of determination (R^2) greater than 0.98 when calibrated with uniaxial tension experimental stress–strain curves of elastomers; other commonly used models had lower R^2 values with 0.65 for Neo-Hookean and 0.59 for Mooney Rivlin. Both hyperelastic and viscoelastic contributions can be used to define the material behavior in a single hyper-viscoelastic material model [18,22,23,29–34] to represent the large-strain behavior and the time-dependent relaxation of the polymer. Each mechanism depends on the CNT weight content, the degree of CNT dispersion throughout the matrix or agglomeration into CNT bundles, and the orientation of the CNTs and CNT bundles in relation to the loading direction. Additionally, thin samples must be characterized to obtain accurate tensile strengths and moduli for thin films [35,36]. Thus, the challenge is to understand how best to represent and understand the global large-strain mechanical behavior of the non-ribbed film while accounting for the rate- or time-dependent effects and the interaction of CNTs in PDMS for various CNT weight fractions.

Hence, we will experimentally characterize various CNT-PDMS compositions to understand how the heterogeneous morphology affects large-strain behavior and how the multi-phase material behavior can accurately and physically represented. Uniaxial mechanical testing was conducted until failure for thin non-ribbed PDMS and CNT-PDMS samples with CNT loadings between 1 wt% (wt%) and 10 wt%. Scanning electron microscopy (SEM) images of the resulting fracture surfaces were obtained to relate the agglomeration, distribution, and alignment of CNTs in PDMS to the ultimate strain, ultimate strength, and global stress–strain behavior. The SEM results also provide insights into how the PDMS and CNT phases interact, and how it is affected by the different weight percentages of the CNT distributions. Finally, a Yeoh hyperelastic and a Yeoh-Prony hyper-viscoelastic material model was optimized from the uniaxial testing data for each CNT-PDMS composition to determine how best to model the multi-phase, heterogeneous material. The Yeoh model was used to describe the large-strain behavior because it accurately captures the response from uniaxial tension testing and requires only three parameters to describe the material behavior [26]. This paper is organized as follows: in Section 2 the procedure for fabricating, testing, and characterization of non-ribbed CNT-PDMS thin-film specimens is detailed; in Section 3 the results from uniaxial testing and SEM are discussed and the thin-films are characterized as hyperelastic and hyper-viscoelastic materials; in Section 4 the findings are summarized.

2. Material and experimental procedures

2.1. Uniaxial mechanical testing of CNT-PDMS

Uniaxial tensile testing was conducted on PDMS and CNT-PDMS samples according to ASTM D638-22. Four CNT loadings were tested: neat PDMS, 1 wt% (wt%) CNT, 3.5 wt% CNT, and 10 wt% CNT. The samples were prepared by mixing the Sylgard 184 silicone elastomer with a 10:1 hardener mixing ratio and the specified weight percent of Nanophite medium-walled CNTs with diameters between 7–12 nm and lengths that varied between 100-200μ m. in a universal planetary mixer to ensure adequate mixing. A three-roll milling machine was also used to disperse CNTs in the PDMS. Aluminum molds were manufactured with dimensions following the ASTM D638-22 Type IV standard: each specimen had a nominal gauge length of 25 mm, gauge width of 6 mm, and thickness of 1.5 mm. The uncured, mixed CNT-PDMS paste was then poured into the molds. For the pure PDMS specimens, the material was first degassed in a vacuum chamber for 30 min and was allowed to cure without the top plate of the mold to avoid bubble generation. For the remaining CNT-PDMS specimens, the mold was closed, and the material was allowed to cure for 60 min at 125 $^{\circ}$ C. Five specimens were made for each CNT loading for a total of twenty specimens.

An Instron 68SC-05 single column table universal testing machine was used to conduct the uniaxial tensile testing of the thin polymer samples. Each specimen was clamped by standard serrated grips to prevent slippage during testing and then subjected to an increasing tension load at a constant loading rate of 5 mm/min until failure. The corresponding nominal strain-rate of the uniaxial testing is 0.0033 s^{-1} based on the sample dimensions. The engineering strain and stress were obtained for each sample.

2.2. Scanning electron microscopy (SEM) imaging

The CNT-PDMS morphology and the damage modes of the nanocomposite was characterized using SEM. A Hitachi SU8700 field emission SEM was used, which allows for ultra-high-resolution imaging at low electron emission energies on insulating samples with no conductive coating. Since the CNT-PDMS samples are non-conductive compared to typical SEM samples a low voltage of 100 V with a current of 91.5 mA and rapid image capturing was used to manage the sample charge and minimize damage to the samples.

SEM imaging was used to investigate the distribution, alignment, and agglomeration of CNTs within the PDMS at several length scales for three CNT loadings: 1 wt%, 3.5 wt%, and 10 wt%. Neat PDMS was also imaged to validate that the samples did not contain voids. The cross-section of the fracture surface produced by the experimental uniaxial testing in Section 2.1 was analyzed to understand the effect of CNTs on the mode of fracture. Magnification levels between 250 and 50,000 were used to view details ranging from the fracture surface texture to the orientation of individual CNTs. Images were also obtained using the electron backscatter detector of the Hitachi SU8700 instrument to better view the sample texture resulting from fracture.

2.3. Hyperelastic and hyper-viscoelastic material models for CNT-PDMS

The Yeoh hyperelastic material model for the uniaxial stress is given by

$$\sigma_{Yeoh} = 2\left(\lambda_1 - \frac{1}{\lambda_1^2}\right)\left(C_{10} + 2C_{20}(I_1 - 3) + 3C_{30}(I_1 - 3)^2\right), \# \quad (1)$$

where λ_1 is the first principal stretch imposed during uniaxial tensile testing and I_1 is the first stretch invariant given by $I_1 = \lambda_1^2 + 2/\lambda_1$ [37,38]. The parameters C_{10}, C_{20}, and C_{30} are obtained by optimizing the material model using experimental data.

The viscoelastic stress contributions are represented by Prony series, a generalized Maxwell model consisting of exponential decaying terms, whose n-term time-dependent relaxation modulus, E_R, is given by

$$E_R(t) = E_0 \sum_{i=1}^{n}\left(1 - g_i \exp\left(-\frac{t}{\tau_i}\right)\right), \# \quad (2)$$

where E_0 is the instantaneous elongation modulus and g_i is the relaxation coefficient corresponding to the relaxation time constant τ_i. Each g_i is bounded between 0 (no relaxation) and 1 (full relaxation) and the sum $\sum_{i=1}^{n} g_i$ is also bounded between 0 and 1.

The total uniaxial stress, σ, for large-strain viscoelasticity is obtained by

$$\sigma(t) = \int_{\infty}^{t} E_R(t-\tau)\frac{d\epsilon(\tau)}{d\tau}d\tau\# \tag{3}$$

where ϵ is the uniaxial strain. Evaluating the integral, substituting $g_R(t) = E_R(t)/E_0$ from Equation (2) as the non-dimensional viscoelastic relaxation, and defining $\sigma_{Yeoh}(\epsilon(t)) = E_0\epsilon(t)$, we obtain the total stress as a function of time as

$$\sigma(t) = \sigma_{Yeoh}(\epsilon(t)) - \int_{0}^{t} \dot{g}_R(t-\tau)\sigma_{Yeoh}(\epsilon(\tau))d\tau.\# \tag{4}$$

By rearranging Equation (4), the combined hyperelastic and viscoelastic stress components gives the uniaxial stress at time t as

$$\sigma(t) = \sigma_{Yeoh}(t) - \sigma_{visc}(t),\# \tag{5}$$

where σ_{visc} is the viscoelastic stress dissipation [31–34]. At time $t + \Delta t$, this gives

$$\sigma(t+\Delta t) = \sigma_{Yeoh}(t+\Delta t) - \sigma_{visc}(t+\Delta t) = \sigma_{Yeoh}(t+\Delta t) - \sum_{i=1}^{n}\sigma_{visc}^{i}(t+\Delta t) \tag{6}$$

where the contribution from the i-th Prony series term is obtained by approximating the integral in Equation (4) as

$$\sigma_{visc}^{i}(t+\Delta t) = \exp\left(-\frac{\Delta t}{\tau_i}\right)\sigma_{visc}^{i}(t) + g_i\sigma_{Yeoh}(t)\left(1-\exp\left(-\frac{\Delta t}{\tau_i}\right)\right) + g_i\frac{\Delta\sigma_{Yeoh}}{\Delta t}\left((\Delta t-\tau_i) + \tau_i\exp\left(-\frac{\Delta t}{\tau_i}\right)\right),\# \tag{7}$$

which was adapted [31].

A constrained interior-point optimization routine was used to obtain the three hyperelastic material model parameters and the Prony relaxation coefficients. The relaxation coefficients were bounded between zero and one, and the total relaxation was bounded between zero and some maximum allowable relaxation factor, $\eta_{relax,max}$, less than unity. The typical long-term relaxation of PDMS is 80 % of the instantaneous value [5,39], so $\eta_{relax,max} = 0.8$ for the hyper-viscoelastic material model optimization. For the hyperelastic material model, the same optimization procedure was used with $\eta_{relax,max} = 0$ to enforce no relaxation. Constraints were not imposed on the Yeoh coefficients. The root-mean-square-error (RMSE) between the model and the experimental uniaxial tensile testing measurements was minimized for each CNT-PDMS composition to obtain the material model parameters. To ensure that the ultimate strength occurs at the ultimate strain for each material, a weight factor was applied to the residuals of the ultimate strength.

3. Results and discussion

The non-ribbed CNT-PDMS samples were prepared for uniaxial tensile testing with varying CNT content to understand how the addition of CNTs affects the large-strain mechanical behavior. SEM micrographs were captured to analyze the fracture surface of each sample, which provided information on the mode of failure and the dispersion, alignment, and agglomeration of CNTs within the PDMS matrix. The CNT-PDMS morphology of the fracture surface was related to the surface behaviors of thin-films for multifunctional applications, with an emphasis on superhydrophobicity and drag reduction. Each CNT-PDMS composition was characterized as a combination of a hyperelastic and a hyper-viscoelastic material. The hyper-viscoelastic material models physically account for the large-strain and rate-dependent behavior of the PDMS and CNT-PDMS thin-films than the hyperelastic material models. Hence, as the results have indicated, this rate-dependent behavior can be used to accurately represent the behavior of CNT-PDMS systems.

3.1. Uniaxial mechanical testing of CNT-PDMS thin-films

Uniaxial tensile testing specimens of each material composition were fabricated according to the procedure outlined in Section 2.1 to understand how increasing the CNT content affects the mechanical behavior of non-ribbed CNT-PDMS thin-film systems. Each specimen was tested in uniaxial tension to obtain the global stress–strain behavior to failure. Fig. 1 shows one sample of each composition after testing.

The fractured samples shown in Fig. 1 are representative of the uniaxial tension behavior for their respective material compositions. The neat PDMS (0 wt% CNT) sample, shown on the left, recovered much of its original shape after fracture, as evidenced by negligible necking through the gauge length. The 1 wt% and 3.5 wt% CNT samples also lack a necking region. The 10 wt% sample, however, shows considerable deformation within the gage length since it is no longer straight, compared to the other samples in Fig. 1. The 10 wt% sample was also elongated compared to the other samples, which suggests it had undergone more plastic deformation during testing. Each tab shows small circular imprints from the grips, which validates that the grip-strength was high enough to prevent the specimens from slipping when subjected to a uniaxial tension load.

The average ultimate engineering strain and strength were obtained from the five specimens of each material with the corresponding standard deviations (Fig. 2). By accurately characterizing the material strength, failure criteria for ribbed thin-film systems can be obtained to improve the design of new material systems, such as ribbed CNT-PDMS systems.

From Fig. 2, there is no statistically significant change in ultimate strain with respect to CNT loading. The ultimate strength, however, had a statistically significant increase with respect to increasing CNT loading. The high-strength and high-modulus elastic CNT fillers increased the overall strength of the material, and the PDMS matrix allowed for effective stress-transfer between neighboring CNTs. At 10 wt %, the standard deviation for the ultimate strain is one-third of the ultimate strain value, which suggests the difficulty with reliably incorporating the high weight fraction of CNTs in the PDMS matrix, and this is an indication of as the weight percentage increases, interactions between the CNTs and the PDMS increases, which can result in inconsistent load transfers [14].

The tensile strengths in Fig. 2 are up to three times larger than those reported [40] for identical CNT-PDMS compositions, though the difference is likely attributed to different sample thicknesses which has been reported to affect the elongation modulus and ultimate strength of thin-films [35,36]. Since the characterization of these non-ribbed CNT-PDMS samples will inform the design of ribbed thin-film systems, the

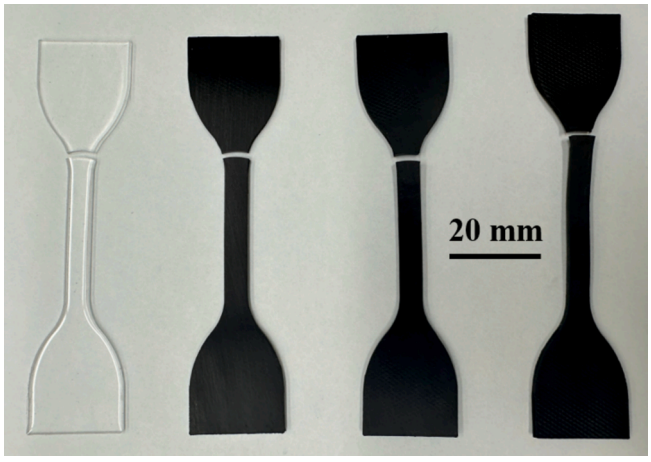

Fig. 1. Non-ribbed PDMS tensile test specimens with CNT loadings, from left to right, of 0 wt% (wt%), 1 wt%, 3.5 wt%, and 10 wt% fabricated according to ASTM D638-22 specifications and subjected to uniaxial tension to failure.

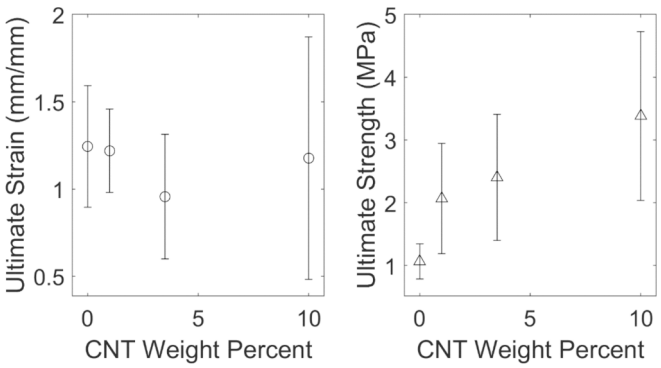

Fig. 2. Ultimate engineering strain and ultimate engineering strength with respect to CNT weight percent in PDMS obtained from the average of five samples with error bars indicating two standard deviations.

ultimate strain and strength in Fig. 2 can be used to represent the material behavior.

3.2. CNT-PDMS surface morphology from SEM measurements

SEM was used to further understand and characterize how the addition of CNTs in PDMS affects the deformation and damage modes during large-strain uniaxial loading. The fracture surface of each sample from Fig. 1 was analyzed to understand the agglomeration, dispersion, and orientation of the CNTs for each material composition and to provide insight on the mode of fracture. Despite the ultra-high-resolution capabilities of the Hitachi SU8700 field emission SEM, the resolution is limited by the beam-material interaction. PDMS exhibits significant charging challenges and is susceptible to damage from the electron dose. This allows for high resolution images of the surface morphology at low beam energies, which manages charging and reduces damage.

The fracture surface of non-ribbed PDMS was observed under SEM (Fig. 3). The surface appears featureless in part due to the non-conductive material properties that make SEM imaging difficult, but also due to the flat fractured topography and the absence of voids indicating the adequate molding of the PDMS thin-film due to degassing as discussed in Section 2.1.

The fracture surfaces of PDMS with 1 wt% and 3.5 wt% CNT were also observed at low and mid-powered magnification using SEM (Fig. 4). The addition of CNTs provides sufficient texture on the fracture surface and increases the conductivity of the samples to makes SEM micrographs obtainable despite charging.

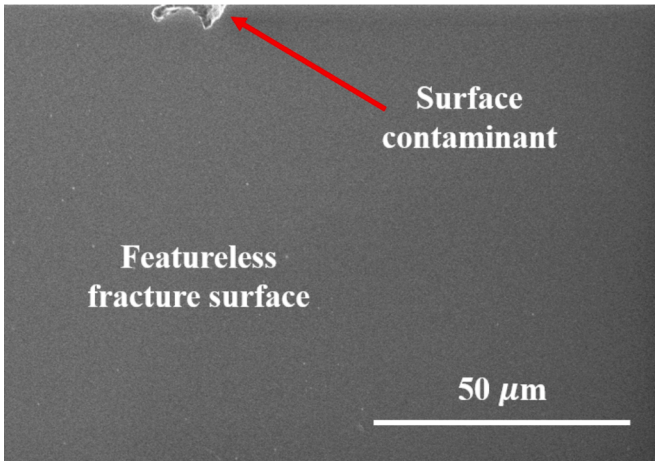

Fig. 3. Scanning electron microscopy (SEM) micrograph of fracture surface at low magnification for neat PDMS obtained using electron beam of 100 V. The texture of the sample is featureless apart from a surface contaminant shown to demonstrate that the material is focused in the SEM.

In Fig. 4a-b, the fracture surface of both material compositions indicates brittle-like fracture, though the topography is more varied than in neat PDMS (Fig. 3) due to the incorporation of CNT bundles. Unlike neat PDMS, the 1 wt% and 3.5 wt% CNT materials were not degassed during the specimen fabrication step in Section 2.1, however, there is no sign of voids in either material. The dark regions in Fig. 4b are polymer-rich and likely locations for local damage to initiate given the lower relative strength of the polymer chains compared to the CNT-polymer bundles. The fracture surface exhibits uniform deformation, similar to other materials such as high-strength metals undergoing low strain rates (10^{-3} s^{-1}) [41].

Fig. 4c-d provide better insights into the heterogeneity of the CNT-PDMS system, namely the agglomeration and distribution of the CNTs. The lighter regions, in general, are bundles of CNTs [37]; the darker regions are PDMS. Bright horizontal streaks appear in Fig. 4c-d because of the highly charged material, even at the low beam energy. The high surface energy of the CNTs cause them to agglomerate into pockets or bundles rather than disperse evenly and randomly in the PDMS. The presence of these bundles explains why the strengthening of the CNTs is not as high as homogenization techniques such as rule of mixtures or micromechanical models that neglect an interphase region would suggest since the bundle has a lower strength than the individual CNT [17,24,25,42–44]. Though individual CNTs agglomerate into bundles, these multi-phase CNT bundles can reasonably be assumed to be distributed uniformly within the PDMS. The 3.5 wt% CNT material in Fig. 4d shows a similar distribution as the 1 wt% CNT material in Fig. 4c, but with a higher density of CNT bundles. This uniform dispersion provides justification for homogenization techniques when the macro-scale material behavior is considered.

PDMS with 10 wt% CNT had excessive charging. A micrograph was obtained with the backscatter electron middle detector of the Hitachi (Fig. 5) at high magnification to better understand the topography of the fracture surface.

The backscatter electron image (Fig. 5) shows the highly irregular fracture surface of the 10 wt% CNT material, which is indicative of a more ductile failure mode than for CNT-PDMS compositions with lower CNT loadings. The expanded region in Fig. 5 shows individual CNTs being pulled from the PDMS matrix at the peaks of the fracture surface. CNT pullout is a non-reversible mode of deformation in CNT-polymer systems that increases the toughness and occurs when the bonding or cohesion strength between the filler and the matrix is less than the shear stress subjected to the CNT-polymer interface. The likelihood of CNT pullout increases with increasing CNT content because the high concentration of CNT bundles, as observed in Fig. 5, begin to act as defects rather than strengthening mechanisms [14,40]; the polymer chains are not capable of wetting the individual CNTs fully.

Low to high magnification SEM images of PDMS with CNT contents between 1 wt% and 10 wt% were obtained that show the CNTs are agglomerated into well-distributed CNT bundles throughout the PDMS (Figs. 4 and 5). The orientation, waviness, and damage of individual CNTs, however, requires ultra-high magnification to be observed (Fig. 6). Knowledge of the CNT orientations and misorientations provides insight into the validity of isotropic material assumptions. Excessive CNT waviness or damage indicates a decrease in achievable strengthening of the composite resulting from the fabrication process [45].

The SEM images in Fig. 6 are consistent with the observations and measurements [46,47] for CNT-PDMS and similar CNT-polymer systems [24,29,45,48,49]. In Fig. 6a-c, the effect of adding CNTs to PDMS is clear by the increase of fiber density. At low weight fractions (Fig. 6a) there exists regions of PDMS that do not have a large presence of CNTs or CNT bundles, in which the stress is transferred through the lower strength matrix only. As the CNT content increases to 3.5 wt% (Fig. 6b), there are fewer regions of pure PDMS and the heterogenous microstructure allows for stress to transfer shorter distances through the PDMS to adjacent CNT

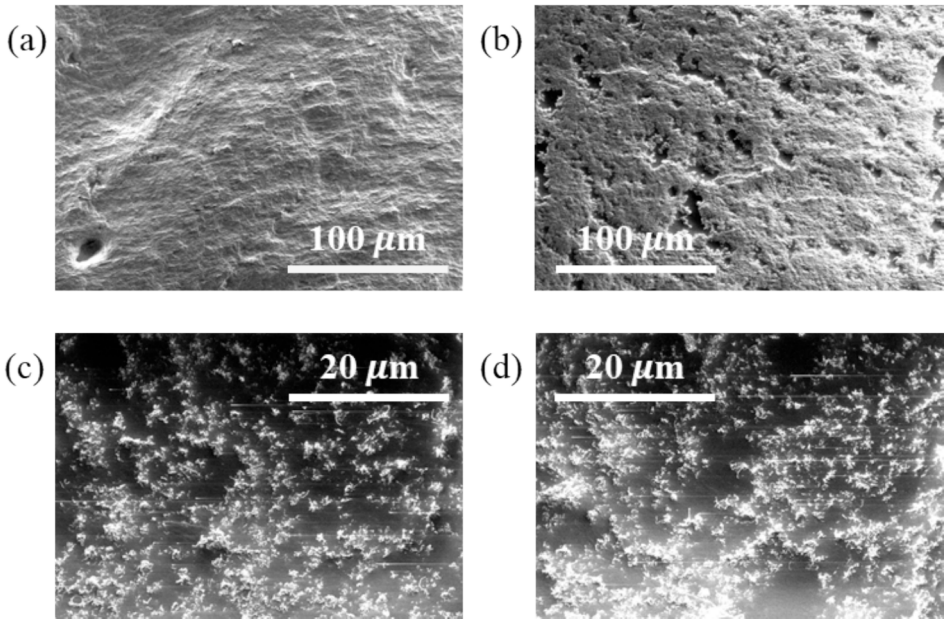

Fig. 4. Scanning electron microscopy micrograph of fracture surface at low magnification for (a) 1 wt% and (b) 3.5 wt% CNT and at higher magnification for (c) 1 wt % and (d) 3.5 wt% CNT obtained using electron beam of 100 V. The texture of the two samples is rough but suggests a brittle-like fracture of the heterogenous material. The lighter regions in (c) and (d) indicate areas of high CNT concentration.

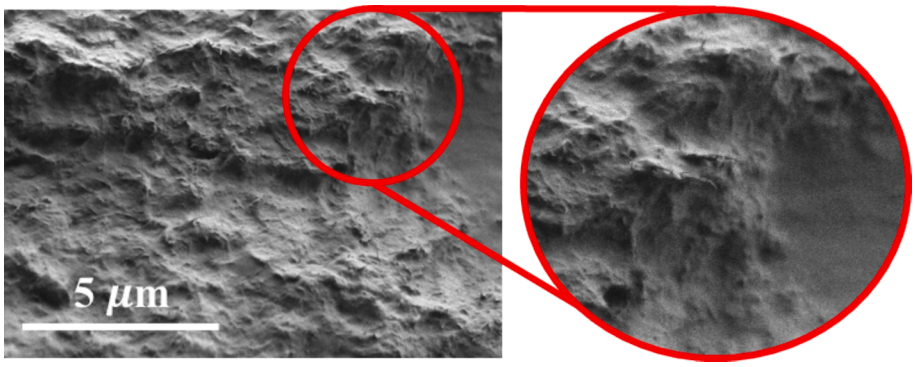

Fig. 5. Scanning electron microscopy (SEM) backscatter micrograph of fracture surface for 10 wt% CNT at high magnification obtained using electron beam of 100 V showing CNT pullout.

bundles. The SEM micrograph of CNT-PDMS with 10 wt% CNT (Fig. 6c) demonstrates how little PDMS remains between CNT bundles, which suggests that the material has difficulty transferring the uniaxial tensile load from one bundle to another and that some regions may not be encapsulated by enough polymer. The dark lines in Fig. 6c indicate damage from taking images; the damage pattern is consistent with the raster scan path—a left vertical line with rightward horizontal forks. The damage helps demonstrate the difficultly of imaging a polymer, despite the low electron dose enabled by using a low-voltage field emission SEM.

At higher magnification, individual CNTs can be clearly seen (Fig. 6d-f), which provided information on the orientation and defect nature of the CNT-PDMS. There exists CNTs within the fracture surface for all three CNT loadings that exhibit kinks at an angle of at least 90 °, consistent with SEM images from [45]. Within a given CNT bundle, the CNTs were randomly oriented. This randomness is due to the extensive mixing process outlined in Section 2.1. The randomly oriented CNTs validate that each bundle can be treated as an isotropic effective fiber.

SEM images were obtained to understand how adding CNTs to PDMS affects the microstructure and strengthens the material. The multi-phase and heterogeneous material exhibit superhydrophobic behavior from the hierarchal topography. Though CNTs coalesce into multi-phase agglomerations, the random orientation of CNTs and dispersion of CNT bundles provide justification for treating non-ribbed and ribbed CNT-PDMS thin-film systems as isotropic, homogeneous materials.

3.3. *Large-strain hyperelastic and hyper-viscoelastic material models of CNT-PDMS*

The uniaxial tensile testing in Section 3.1 provides a description of the global mechanical behavior of CNT-PDMS for various compositions; SEM imaging in Section 3.2 improves our understanding of the heterogeneous microstructure and the fracture surface. However, it is still not understood how to best characterize the bulk material behavior for use in ribbed thin-film systems subjected to large strains and strain rates. Several constitutive and phenomenological materials models have been developed to understand the mechanical behavior of polymer and composite materials, such as hyperelasticity and hyper-viscoelasticity. Both material models can predict the material response to uniaxial tension. To understand how best to represent the large-strain mechanical behavior of various CNT-PDMS compositions, a hyperelastic and hyper-viscoelastic material model was obtained for each composition to

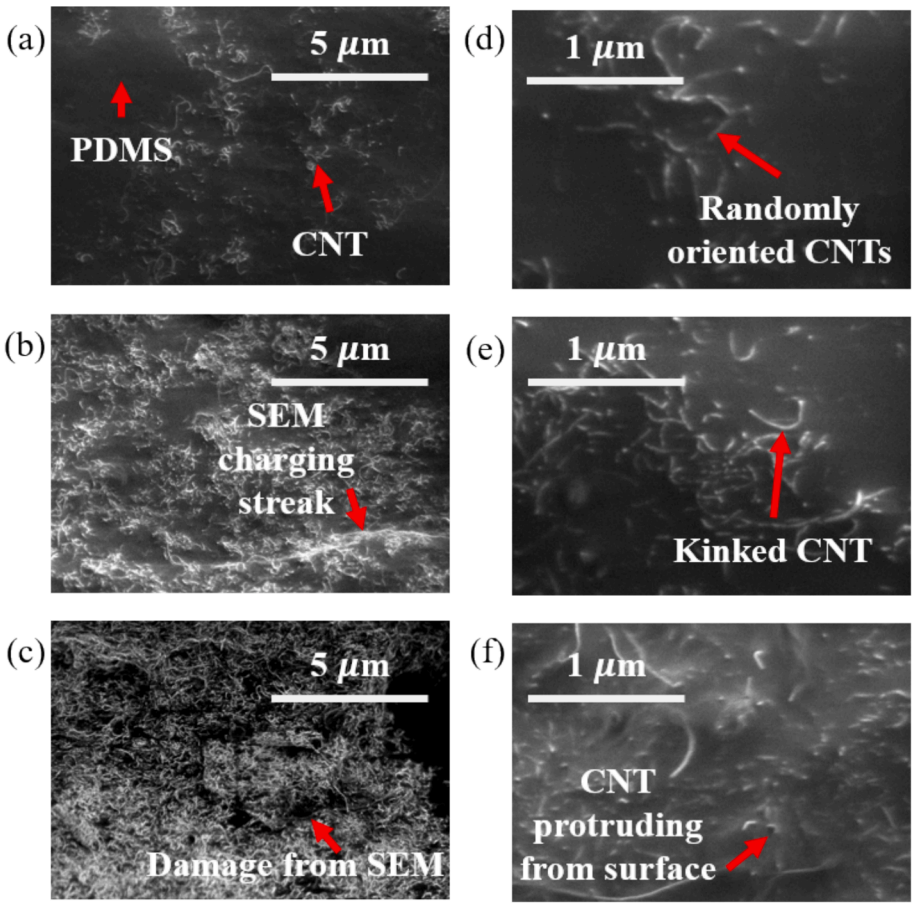

Fig. 6. Scanning electron microscopy (SEM) micrograph of fracture surface at high magnification for (a) 1 wt%, (b) 3.5 wt% and (c) 10 wt% CNT and at ultra-high magnification for (d) 1 wt%, (e) 3.5 wt% and (f) 10 wt% CNT obtained using electron beam of 100 V.

determine the more physically-accurate material model.

First, a Yeoh hyperelastic material model was optimized to represent the material behavior of the experimental stress–strain measurements. For each material composition, the Yeoh material model was obtained from the initialized hyperelastic material model coefficients ($C_{10,init}$ = 0.1, $C_{20,init}$ = 0.01, $C_{30,init}$ = 0.001) for strains up to the ultimate strain. The residuals were obtained for the stress predicted by the model and measured in each of the five specimens. To force the material model to satisfy the ultimate strength, additional residuals between the maximum predicted stress and the average ultimate strength were added to the residual vector with a weight factor. This weight factor was manually adjusted to obtain an appropriate material model that adequately accounted for the ultimate strength without obscuring the global stress–strain behavior. The root-mean-square-error (RMSE) was obtained from the residual vector and a constrained interior-point optimization procedure discussed in Section 2.3 was conducted to update the hyperelastic material model coefficients for each material composition.

Thus, the optimization problem statement was to find C_{10}, C_{20}, and C_{30} that minimize the root mean square error, $RMSE = \sqrt{\frac{1}{n}\left(\sigma_{experiments} - \sigma_{Yeoh}\right)^2}$, for each material composition where the uniaxial stress history of each sample was appended into a single column vector, $\sigma_{experiments}$, and the corresponding uniaxial stress predicted by the Yeoh material model was appended into a column vector, σ_{Yeoh}, both of length n. The Yeoh material model for the four CNT-PDMS compositions are summarized in Table 1.

Similarly, the Yeoh-Prony hyper-viscoelastic material model was optimized for each material composition. Neat PDMS has been characterized as viscoelastic [5,22,23,39] so the composite material is also expected to exhibit viscoelastic relaxation. The same optimization procedure from Section 2.3 was used, though the material was allowed to relax according to Equation (2) assuming a constant nominal strain-rate as specified in Section 2.1 to account for the time-dependency of the mechanical testing procedure. Thus, the three Yeoh coefficients (C_{10}, C_{20}, C_{30}) and three Prony relaxation coefficients (g_1, g_2, g_3) were obtained for each material that minimize the RMSE. The Prony time constants, τ_i, were 1, 10, and 100 s. The total time of each uniaxial tension test was between 220 and 520 s, so the choice of τ_i captures the fast and slow relaxation mechanisms that were observed during testing. The optimized hyper-viscoelastic material model coefficients are summarized in Table 2 with the corresponding RMSE for each CNT-PDMS composition.

The first coefficient in the Yeoh material model, C_{10}, is interpreted as approximately half of the shear modulus of the material [28]. Based on Table 1, the instantaneous elongation modulus for the hyperelastic

Table 1
Hyperelastic Yeoh material model coefficients of four compositions of CNT-PDMS obtained by constrained optimization routine with root-mean-square-error.

CNT Weight Percent (wt% CNT)	Yeoh Hyperelastic Material Model Coefficients			Root-Mean-Square-Error (MPa)
	C_{10}(MPa)	C_{20}(MPa)	C_{30}(MPa)	
0	0.1303	0.0185	0.0013	0.0078
1	0.2713	0.0321	0.0027	0.0111
3.5	0.5330	0.0299	0.0062	0.0043
10	0.8715	0.0082	−0.0024	0.0811

Table 2
Hyper-viscoelastic Yeoh-Prony material model coefficients of four compositions of CNT-PDMS obtained by constrained optimization routine with root-mean-square-error.

CNT Weight Percent (wt% CNT)	Yeoh Hyperelastic Coefficients			Prony Viscoelastic Relaxation Coefficients			Root-Mean-Square-Error (MPa)
	C_{10}(MPa)	C_{20}(MPa)	C_{30}(MPa)	g_1	g_2	g_3	
0	0.2133	0.0634	0.0016	0.0654	0.1509	0.5679	0.0078
1	0.4010	0.0888	0.0016	0.1510	0.0582	0.3826	0.0111
3.5	0.6320	0.0372	0.0069	0.1487	0.0100	0.0033	0.0043
10	2.2985	0.1142	−0.0242	0.4144	0.2377	0.0004	0.0806

material models, assuming an incompressible material, ranges between 0.75 MPa and 5.25 MPa for the various compositions. These values are slightly lower than those that have been experimentally obtained; 1 MPa for 0 wt%, 5.7 MPa for 3.5 wt%, and 10 MPa for 10 wt% CNT [40]. The hyperelastic material model from Table 1 underestimates the stress in the small-strain regime, but by including the viscoelastic relaxation, the magnitude of the hyperelastic coefficient C_{10} increases (Table 2) to account for the rate-dependent behavior. The estimated elongation modulus from C_{10} for the hyper-viscoelastic material model is 1.28 MPa for 0 wt%, 2.41 MPa for 1 wt%, 3.79 MPa for 3.5 wt%, and 13.79 MPa for 10 wt% CNT, which are consistent with reported values [40]. Thus, the hyper-viscoelastic material models accurately capture the mechanical behavior in the small-strain regime because they account for the rate-dependent relaxation of the polymer, the interactions between CNTs and polymer chains, and the uniaxial testing quasi-static rates.

The second and third coefficients of the Yeoh hyperelastic model, C_{20} and C_{30}, describe the stress–strain response in the mid- and large-strain regimes. In both the hyperelastic and hyper-viscoelastic material model formulations (Tables 1-2), C_{30} increases with increasing CNT loading up to 3.5 wt%; after which, C_{30} is negative at 10 wt% CNT. The most likely cause for the stress increasing in the large-strain regime is the straightening of the curved CNTs observed in Fig. 6, that provide additional stiffness to the thin samples [50]. The 10 wt% CNT material begins to plateau in the large-strain regime, which is consistent with [14] and is likely due to poor bonding between the PDMS and CNT bundles or the separation of large CNT agglomerations that are not properly adhered to the PDMS, as observed in SEM images (Fig. 6).

The Yeoh hyperelastic material behavior is compared to the five specimens for each material in Fig. 7. Here, the addition of CNTs in the PDMS increases the ultimate strength for all compositions. All four material models show good agreement with the experimental uniaxial tension data. Similarly, the Yeoh-Prony hyper-viscoelastic material model behavior is compared to the uniaxial testing results for each material in Fig. 8. As with Fig. 7, the addition of CNTs in the PDMS increases the initial stress–strain slope and increases the ultimate strength for CNT loadings up to 10 wt%. Both the hyperelastic and hyper-viscoelastic material models can predict the mechanical behavior of CNT-PDMS for various compositions.

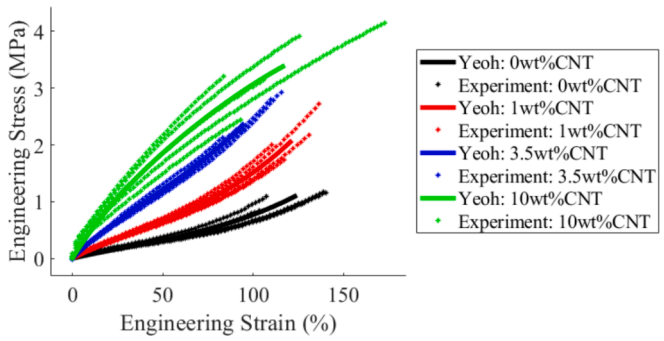

Fig. 7. Yeoh hyperelastic material model for four material compositions of CNT-PDMS optimized from five uniaxial tension experiments of each composition.

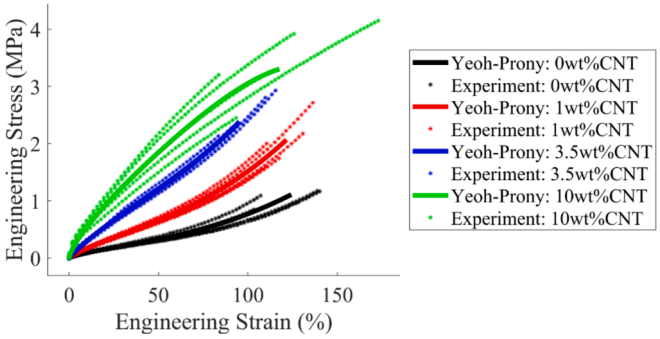

Fig. 8. Yeoh-Prony hyper-viscoelastic material model for four material compositions of CNT-PDMS optimized from five uniaxial tension experiments of each composition.

The RMSE for the hyperelastic and hyper-viscoelastic material models are comparable for each material composition. Though, since the hyper-viscoelastic material model accounts for the loading rate of the uniaxial tests and the rate-dependent viscoelastic material relaxation, it is likely the more accurate prediction of the mechanical behavior and can be used reliably for low strain-rate responses on the order of 10^{-3} s^{-1}, similar to the uniaxial testing strain-rate given in Section 2.1. Thus, the hyper-viscoelastic material models better represent the global stress–-strain behavior.

The ideal CNT-PDMS composition for multifunctional systems exhibiting large-strain and high-strength behaviors is between 3.5 wt% and 10 wt% CNT. Though the tensile strength increases with increasing CNT loading, as suggested in Fig. 2, it does so with diminishing returns. SEM micrographs indicate that CNTs agglomerate into randomly oriented, well-dispersed bundles; the micrographs support observations of hydrophobic surface behaviors because of the hierarchal CNT-PDMS topography. The global stress–strain mechanical behavior (Figs. 7 and 8) suggests that the CNTs no longer act as strengthening mechanisms, but as defects as the CNT loading increases to 10 wt%. Hyper-viscoelastic material models accurately predict the large-strain rate-dependent bulk mechanical behavior of thin CNT-PDMS systems, and can be used to predict the behavior of ribbed thin-film systems.

4. Summary

Large-strain hyperelastic and hyper-viscoelastic material behavior of PDMS and CNT-PDMS samples with various CNT weight percentages were obtained to understand and characterize the effects of CNT loading, agglomeration, dispersion, and alignment on the global and local mechanical behavior and how to physically represent the material behavior. Thin PDMS and CNT-PDMS samples were fabricated and subjected to quasi-static uniaxial testing until failure. The ultimate strain, ultimate strength, and global stress–strain behavior of each CNT-PDMS composition was obtained and related to the CNT content. Increasing the loading content of CNT did not affect the ultimate strain at which the thin samples fractured, though it increased the ultimate strength. The instantaneous elongation modulus of the CNT-PDMS compositions were consistent with experimentally observed

measurements. High-strength elastic CNTs additions to the viscoelastic PDMS significantly increased the material stiffness. CNT-PDMS with CNT loadings between 0 wt% (neat PDMS) and 3.5 wt% exhibited a high rate-increase of stress in the large-strain regime; the stress in PDMS with 10 wt% CNT plateaued in this regime indicating that the material had reached its loading strength of the CNTs.

The fracture surface of each sample was analyzed by SEM to understand the surface morphology and the incorporation of CNTs in the PDMS from the three-roll shear mixing procedure. SEM images of neat PDMS indicated that the material contained no voids. CNT-PDMS with 1 wt% and 3.5 wt% CNT content showed a near-uniform fracture surface, indicating that the failure initiated with failure of the PDMS, whereas CNT-PDMS with 10 wt% CNT showed CNT pullout, which indicates that failure initiated within CNT bundles.

A Yeoh hyperelastic and a Yeoh-Prony hyper-viscoelastic material model were shown to physically represent each material composition to understand how best to model the large-strain bulk mechanical behavior of the multi-phase materials. Both material model formulations can describe the mechanical behavior in response to large-strain loading conditions. The hyper-viscoelastic model, however, also accounts for the rate-dependence, which would make it ideal for ribbed systems, which are subjected to high strain-rate loading conditions during loading.

By relating the hyper-viscoelastic global behavior to SEM micrographs of CNT-polymer systems can aid in establishing validated understanding of the distribution and agglomeration of CNT geometries and orientations within polymer matrix systems. This will enable manufacturers of heterogeneous, structured thin-film materials to predict and control the mechanical and surface behavior for multifunctional applications.

CRediT authorship contribution statement

Matthew Phillips: Methodology, Investigation, Formal analysis, Data curation, Conceptualization. **Pouria Zaghari:** Investigation, Formal analysis. **Jong Eun Ryu:** Project administration, Methodology, Conceptualization. **Mohammed Zikry:** Funding acquisition, Data curation, Conceptualization.

Declaration of competing interest

The authors declare that they have no known competing financial interests or personal relationships that could have appeared to influence the work reported in this paper.

Data availability

Data will be made available on request.

Acknowledgements

The authors were all supported by Grant 2031558 from the National Science Foundation.

The SEM characterization performed at the Analytical Instrumentation Facility (AIF) at North Carolina State University, which is supported by the State of North Carolina and the National Science Foundation (award number ECCS-2025064). The AIF is a member of the North Carolina Research Triangle Nanotechnology Network (RTNN), a site in the National Nanotechnology Coordinated Infrastructure (NNCI).

References

[1] Park S-H, Lee S, Moreira D, Bandaru PR, Han I, Yun D-J. Bioinspired superhydrophobic surfaces, fabricated through simple and scalable roll-to-roll processing. Sci Rep 2015;5:15430. https://doi.org/10.1038/srep15430.

[2] Didarul Islam M, Perera H, Chockalingam S, Phillips M, Chen MJ, Liu Y, et al. Template-free scalable fabrication of linearly periodic microstructures by controlling ribbing defects phenomenon during forward roll coating. Manuf Lett 2022;33: 153–160. doi: 10.1016/j.mfglet.2022.08.001.

[3] Islam MD, Perera H, Black B, Phillips M, Chen M, Hodges G, et al. Template-free scalable fabrication of linearly periodic microstructures by controlling ribbing defects phenomenon in forward roll coating for multifunctional applications. Adv Mater Interfaces 2022;9:2201237. https://doi.org/10.1002/admi.202201237.

[4] Perera H, Black B, Islam MD, Ryu JE, Corder RD, Khan SA. Rheological behavior and roll coating properties of pdms enhanced with multi-walled carbon nanotubes and fumed silica. ACS Appl Eng Mater 2024;2:618–27. https://doi.org/10.1021/acsaenm.3c00698.

[5] Phillips M, Chen M-J, Islam MD, Ryu J, Zikry M. Predicting and Controlling Ribbing Instabilities of Carbon Nanotube–PDMS Thin-Film Systems for Multifunctional Applications. Adv Eng Mater 2023;25:2300582. https://doi.org/10.1002/adem.202300582.

[6] Barahman M, Lyons AM. Ratchetlike slip angle anisotropy on printed superhydrophobic surfaces. Langmuir 2011;27:9902–9. https://doi.org/10.1021/la201222a.

[7] Lang AW, Motta P, Hidalgo P, Westcott M. Bristled shark skin: a microgeometry for boundary layer control? Bioinspir Biomim 2008;3:046005. https://doi.org/10.1088/1748-3182/3/4/046005.

[8] Bhushan B. Lessons from nature for green science and technology: an overview and bioinspired superliquiphobic/philic surfaces. Philos Trans R Soc Math Phys Eng Sci 2019;377:20180274. https://doi.org/10.1098/rsta.2018.0274.

[9] J.H. Lee, J.C. Hyun, Ribbing instability in rigid and deformable forward roll coating flows, Korea-Aust. Rheol. J, (2010) 75-80.

[10] Fields RJ, Ashby MF. Finger-like crack growth in solids and liquids. Philos Mag 1976;33:33–48. https://doi.org/10.1080/14786437608221089.

[11] Liu N, Sun Q, Yang Z, Shan L, Wang Z, Li H. Wrinkled Interfaces: Taking Advantage of Anisotropic Wrinkling to Periodically Pattern Polymer Surfaces. Adv Sci 2023; 10:2207210. https://doi.org/10.1002/advs.202207210.

[12] T. Miyata, K. Tokumaru, F. Tsumori, Combining multi-step imprinting with the in-plane compression method, Jpn. J. Appl. Phys. 59 (2020) SIIJ07. doi: 10.35848/1347-4065/ab79ef.

[13] Siviour CR, Jordan JL. High Strain Rate Mechanics of Polymers: A Review. J Dyn Behav Mater 2016;2:15–32. https://doi.org/10.1007/s40870-016-0052-8.

[14] P. Datta, C. Guha, G. Sarkhel, Mechanical, rheological, and electrical properties of multiwalled carbon nanotube reinforced ASA/Na-ionomer blend, J. Appl. Polym. Sci. 132 (2015) app.42516. doi: 10.1002/app.42516.

[15] Chen Y, Zhao Z, Li D, Guo Z, Dong L. Constitutive modeling for linear viscoelastic fiber-reinforced composites. Compos Struct 2021;263:113679. https://doi.org/10.1016/j.compstruct.2021.113679.

[16] Asadian H, Shelesh-Nezhad K. Simulation of dynamic mechanical and viscoelastic behavior in polymer/clay nanocomposites. Polym Compos 2020;41:817–23. https://doi.org/10.1002/pc.25412.

[17] Hu A, Li X, Ajdari A, Jiang B, Burkhart C, Chen W, et al. Computational analysis of particle reinforced viscoelastic polymer nanocomposites – statistical study of representative volume element. J Mech Phys Solids 2018;114:55–74. https://doi.org/10.1016/j.jmps.2018.02.013.

[18] Pan G, Chen M, Wang Y, Zhang J, Liu L, Zhang L, et al. Hyper-Pseudo-Viscoelastic Model and Parameter Identification for Describing Tensile Recovery Stress-Strain Responses of Rubber Components in TBR. Polymers 2022;15:76. https://doi.org/10.3390/polym15010076.

[19] Yu L, Skov AL. Monolithic growth of partly cured polydimethylsiloxane thin film layers. Polym J 2014;46:123–9. https://doi.org/10.1038/pj.2013.72.

[20] Wang Z, Smith DE. Numerical analysis on viscoelastic creep responses of aligned short fiber reinforced composites. Compos Struct 2019;229:111394. https://doi.org/10.1016/j.compstruct.2019.111394.

[21] He Y, Lu X, Wu D, Zhou M, He G, Zhang J, et al. CNT/PDMS conductive foam-based piezoresistive sensors with low detection limits, excellent durability, and multifunctional sensing capability. Sens Actuators Phys 2023;358. https://doi.org/10.1016/j.sna.2023.114408.

[22] Payne T, Mitchell S, Bibb R, Waters M. Development of novel synthetic muscle tissues for sports impact surrogates. J Mech Behav Biomed Mater 2015;41:357–74. https://doi.org/10.1016/j.jmbbm.2014.08.011.

[23] Payne T, Mitchell S, Bibb R, Waters M. The evaluation of new multi-material human soft tissue simulants for sports impact surrogates. J Mech Behav Biomed Mater 2015;41:336–56. https://doi.org/10.1016/j.jmbbm.2014.09.018.

[24] Sepúlveda AT, Guzman de Villoria R, Viana JC, Pontes AJ, Wardle BL, Rocha LA. Full elastic constitutive relation of non-isotropic aligned-CNT/PDMS flexible nanocomposites. Nanoscale 2013;5:4847. https://doi.org/10.1039/c3nr00753g.

[25] R. Ansari, M.K. Hassanzadeh Aghdam, Micromechanics-based viscoelastic analysis of carbon nanotube-reinforced composites subjected to uniaxial and biaxial loading, Compos. Part B Eng. 90 (2016) 512–522. doi: 10.1016/j.compositesb.2015.10.048.

[26] Melly SK, Liu L, Liu Y, Leng J. A review on material models for isotropic hyperelasticity. Int J Mech Syst Dyn 2021;1:71–88. https://doi.org/10.1002/msd2.12013.

[27] Dal H, Açıkgöz K, Badienia Y. On the Performance of Isotropic Hyperelastic Constitutive Models for Rubber-Like Materials: A State of the Art Review. Appl Mech Rev 2021;73:020802. https://doi.org/10.1115/1.4050978.

[28] Nguyen H-D, Huang S-C. The Uniaxial Stress-Strain Relationship of Hyperelastic Material Models of Rubber Cracks in the Platens of Papermaking Machines Based on Nonlinear Strain and Stress Measurements with the Finite Element Method. Materials 2021;14:7534. https://doi.org/10.3390/ma14247534.

[29] Tas MO, Baker MA, Masteghin MG, Bentz J, Boxshall K, Stolojan V. Highly Stretchable, Directionally Oriented Carbon Nanotube/PDMS Conductive Films

with Enhanced Sensitivity as Wearable Strain Sensors. ACS Appl Mater Interfaces 2019;11:39560–73. https://doi.org/10.1021/acsami.9b13684.
[30] Shim VPW, Yang LM, Lim CT, Law PH. A visco-hyperelastic constitutive model to characterize both tensile and compressive behavior of rubber. J Appl Polym Sci 2004;92:523–31. https://doi.org/10.1002/app.20029.
[31] Bergstrom J. Mechanics of Solid Polymers: Theory and Computational Modeling. 1st ed.,. William Andrew; 2015.
[32] Shojaeifard M. On finite bending of visco-hyperelastic materials: a novel analytical solution and FEM. Acta Mechanica 2020;231:3435–50. https://doi.org/10.1007/s00707-020-02733-4.
[33] Ghoreishy MHR. Determination of the parameters of the Prony series in hyper-viscoelastic material models using the finite element method. Mater Des 2012;35:791–7. https://doi.org/10.1016/j.matdes.2011.05.057.
[34] Ghoreishy MHR, Alimardani M, Mehrabian RZ, Gangali ST. Modeling the hyperviscoelastic behavior of a tire tread compound reinforced by silica and carbon black. J Appl Polym Sci 2013;128:1725–31. https://doi.org/10.1002/app.38242.
[35] Song K, Cho N-K, Park K, Kim C-S. Investigating Mechanical Behaviours of PDMS Films under Cyclic Loading. Polymers 2022;14:2373. https://doi.org/10.3390/polym14122373.
[36] Liu M, Sun J, Sun Y, Bock C, Chen Q. Thickness-dependent mechanical properties of polydimethylsiloxane membranes. J Micromechanics Microengineering 2009;19:035028. https://doi.org/10.1088/0960-1317/19/3/035028.
[37] Arif MF, Kumar S, Gupta TK, Varadarajan KM. Strong linear-piezoresistive-response of carbon nanostructures reinforced hyperelastic polymer nanocomposites. Compos Part Appl Sci Manuf 2018;113:141–9. https://doi.org/10.1016/j.compositesa.2018.07.021.
[38] Yeoh OH. Characterization of Elastic Properties of Carbon-Black-Filled Rubber Vulcanizates. Rubber Chem Technol 1990;63:792–805.
[39] K. Long, J. Brown, A Linear Viscoelastic Model Calibration of Sylgard 184., 2017. doi: 10.2172/1365535.
[40] Du J, Wang L, Shi Y, Zhang F, Hu S, Liu P, et al. Optimized CNT-PDMS Flexible Composite for Attachable Health-Care Device. Sensors 2020;20:4523. https://doi.org/10.3390/s20164523.
[41] Salem HG, Lee WM, Bodelot L, Ravichandran G, Zikry MA. Quasi-Static and High-Strain-Rate Experimental Microstructural Investigation of a High-Strength Aluminum Alloy. Metall Mater Trans A 2012;43:1895–901. https://doi.org/10.1007/s11661-011-1064-6.
[42] Gahruei MH, Golestanian H. Evaluation of effective mechanical properties of nanocomposites reinforced with multiwalled carbon nanotube. Mater Sci Technol 2013;29:1484–91. https://doi.org/10.1179/1743284713Y.0000000312.
[43] Razavi R, Zare Y, Rhee KY. A model for tensile strength of polymer/carbon nanotubes nanocomposites assuming the percolation of interphase regions. Colloids Surf Physicochem Eng Asp 2018;538:148–54. https://doi.org/10.1016/j.colsurfa.2017.10.063.
[44] Figiel Ł. Effect of the interphase on large deformation behaviour of polymer–clay nanocomposites near the glass transition: 2D RVE computational modelling. Comput Mater Sci 2014;84:244–54. https://doi.org/10.1016/j.commatsci.2013.12.012.
[45] Motamedi M, Eskandari M, Yeganeh M. Effect of straight and wavy carbon nanotube on the reinforcement modulus in nonlinear elastic matrix nanocomposites. Mater Des 2012;34:603–8. https://doi.org/10.1016/j.matdes.2011.05.013.
[46] Kim D, Yun K-S. Patterning of carbon nanotube films on PDMS using SU-8 microstructures. Microsyst Technol 2013;19:743–8. https://doi.org/10.1007/s00542-012-1677-8.
[47] He Y, Wu D, Zhou M, Zheng Y, Wang T, Lu C, et al. Wearable Strain Sensors Based on a Porous Polydimethylsiloxane Hybrid with Carbon Nanotubes and Graphene. ACS Appl Mater Interfaces 2021;13:15572–83. https://doi.org/10.1021/acsami.0c22823.
[48] Manchado MAL, Valentini L, Biagiotti J, Kenny JM. Thermal and mechanical properties of single-walled carbon nanotubes–polypropylene composites prepared by melt processing. Carbon 2005;43:1499–505. https://doi.org/10.1016/j.carbon.2005.01.031.
[49] Nguyen-Tran H-D, Hoang V-T, Do V-T, Chun D-M, Yum Y-J. Effect of Multiwalled Carbon Nanotubes on the Mechanical Properties of Carbon Fiber-Reinforced Polyamide-6/Polypropylene Composites for Lightweight Automotive Parts. Materials 2018;11:429. https://doi.org/10.3390/ma11030429.
[50] Paul J, Sindhu S, Nurmawati MH, Valiyaveettil S. Mechanics of prestressed polydimethylsiloxane-carbon nanotube composite. Appl Phys Lett 2006;89:184101. https://doi.org/10.1063/1.2372447.